

Emergent SU(3) magnons and thermal Hall effect in the antiferromagnetic skyrmion lattice

Hikaru Takeda^{1*,*}, Masataka Kawano^{2*,†}, Kyo Tamura¹, Masatoshi Akazawa¹, Jian Yan¹, Takeshi Waki³, Hiroyuki Nakamura³, Kazuki Sato⁴, Yasuo Narumi⁴, Masayuki Hagiwara⁴, Minoru Yamashita¹, and Chisa Hotta⁵

¹*Institute for Solid State Physics, University of Tokyo, Kashiwa, 277-8581, Japan*

²*Department of Physics, Technical University of Munich, 85748 Garching, Germany*

³*Department of Materials Science and Engineering, Kyoto University, Kyoto 606-8501, Japan*

⁴*Center for Advanced High Magnetic Field Science (AHMF),*

Graduate School of Science, Osaka University, Toyonaka, Osaka 560-0043, Japan and

⁵*Department of Basic Science, University of Tokyo, Meguro-ku, Tokyo 153-8902, Japan*

Complexity of quantum phases of matter is often understood by the underlying gauge structures, as was recognized by the \mathbb{Z}_2 and U(1) gauge theory description of spin liquid in frustrated magnets. Anomalous Hall effect of conducting electrons can intrinsically arise from U(1) gauges expressing the spatial modulation of ferromagnetic moments or from SU(2) gauges representing the spin-orbit coupling effect. Similarly, in insulating ferro and antiferromagnets, the magnon excitations can contribute to anomalous transports by feeling the U(1) and SU(2) gauges arising from the features of ordered moments or interactions. In this work, we report the emergent higher rank SU(3) gauge structure in the magnon transport based on the thermal conductivity measurements of MnSc₂S₄ in an applied field up to 14 T. The thermal Hall coefficient takes a substantial value when the material enters a three-sublattice antiferromagnetic skyrmion phase, which is confirmed by the large-scale spin wave theory. The excited magnons are dressed with SU(3) gauge field, which is a mixture of three species of U(1) gauge fields originating from the slowly varying magnetic moments on these sublattices.

I. INTRODUCTION

Quantum phases of matter are very often complex and require mathematical ingenuity to clarify the nature of emergent phenomena. One famous example is the bound states of kinks that appear as gapped low energy excitations of the seemingly simple Ising spin system in CoNb₂O₆, which turned out to follow an emergent E₈ exceptional Lie algebra symmetry¹ based on the integrable field theory². Indeed, there are several other cases that effective theories explaining the low-energy excitations of interesting quantum phases are not the simple bosonic or quasi-particle ones but are those subject to gauge fields. In the Kitaev model, the spin-1/2 degrees of freedom separate into Majorana fermions and fluxes of an emergent \mathbb{Z}_2 gauge field³. The half-quantized thermal Hall conductivity reported in α -RuCl₃ is argued as being carried by these fractionalized Majorana fermions⁴⁻⁷. In the pyrochlore systems, quantum fluctuations transform a spin ice state to a U(1) spin liquid phase characterized by the emergent lattice electrodynamics with U(1) global gauge symmetry. The masked pinch point singularities of inelastic scattering signature in Pr₂Zr₂O₇ is considered relevant to this state hosting a monopole excitation⁸.

When one refers to the gauges in material solids, they are quantum mechanical as there is always redundancy in the description of phases of wave functions of the related particles. While these gauges never break their symmetries in the way that the lattice symmetries mark the phase transitions, the related gauge invariants can play another important role. For example, the spin-orbit coupling of electrons or the non-coplanar structured lo-

calized magnetic moments can bear an emergent U(1) gauge field. This gauge field represents the fictitious magnetic field that bends the motion of charges and yields an anomalous Hall effect⁹⁻¹². There, the quantized Hall resistance is explained by the gauge invariant referred to as a Chern number. In chiral magnets such as MnSi^{13,14} that are also good metals, the conduction electrons feel an emergent gauge field as they travel through the spatially varying spin-textures and contribute to the topological Hall effect^{15,16}.

Magnons in insulating magnets are simple bosonic excitations but can also carry a U(1) gauge; the thermal Hall effect in ferromagnetic insulators¹⁷ was the first to report the topological transport of magnons due to U(1) gauge field. Theories showed that the antisymmetric Dzyaloshinskii-Moriya (DM) spin exchange interactions or the non-coplanar structures of ordered moments can be represented by the gauge that bears the Berry curvature in the energy bands¹⁸⁻²¹. Furthermore, in the insulating versions of skyrmions, GaV₄Se₈²², the magnon thermal Hall effect is explained by the U(1) gauge fields²³ similarly to the cases of metallic skyrmions.

One may thus expect that a more abundant gauge structure may appear successively in the transport phenomena. However, even for simple two-sublattice insulating antiferromagnets in noncentrosymmetric crystals where the U(1) gauge picture is not applicable, it was only recently recognized that there can be another route using the SU(2) gauge field to have the anomalous thermal Hall effect²⁶⁻²⁸.

Here, we report the experimental observation of the thermal Hall effect in the three-sublattice antiferromag-

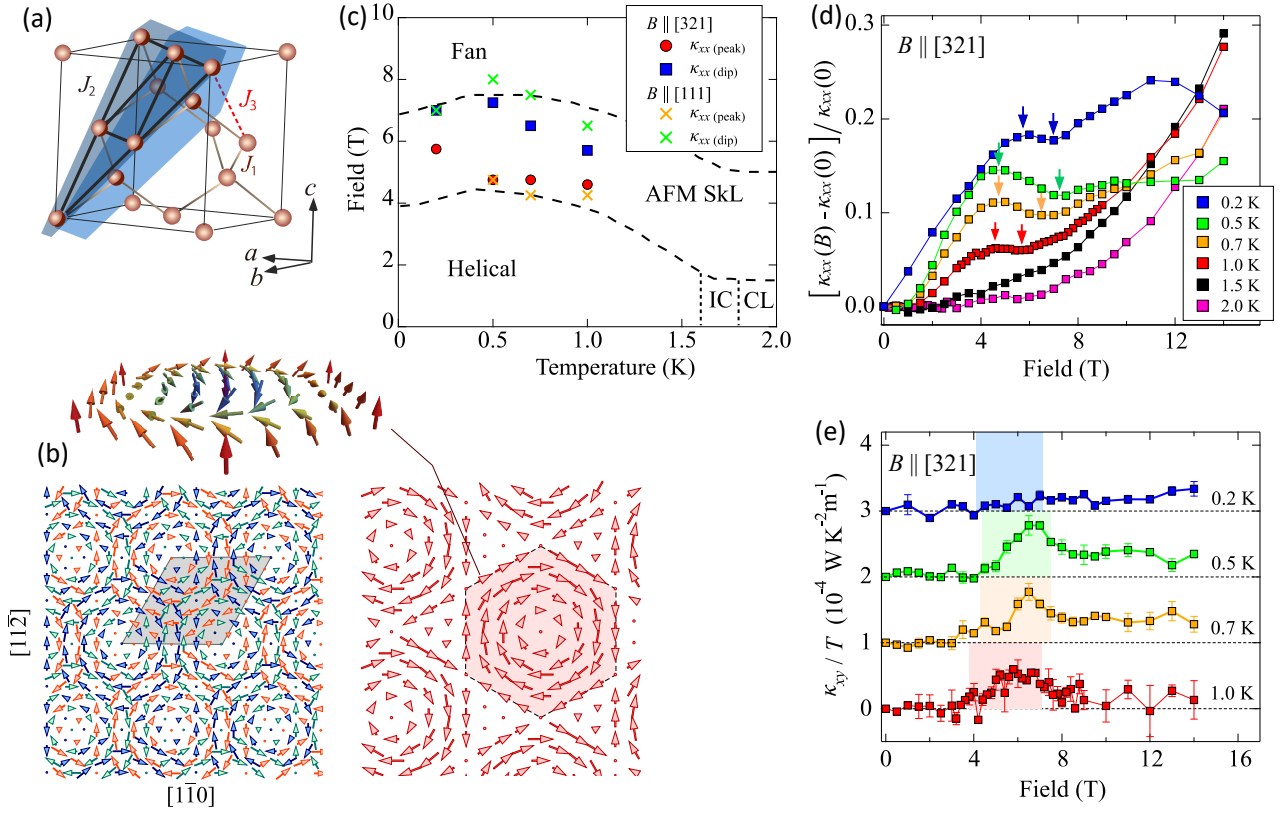


FIG. 1. (a) Diamond lattice formed by Mn^{2+} ions (red circles) in MnSc_2S_4 . The blue planes represent $[111]$ planes where the Mn^{2+} ions form a triangular lattice. The magnetic unit cell of AFM-SkL consists of six triangular layers. (b) Schematic figure of the AFM-SkL state in MnSc_2S_4 viewed along the $[111]$ direction (left-bottom panel), where the spins on three different sublattices are shown in different colors, and the unit cell on that layer including 64 sites are shown. Spins on one of the sublattices forming a ferromagnetic skyrmion lattice are extracted on the right panel, and its hexagonal unit is shown in more detail on the top panel. (c) Magnetic field B versus temperature T phase diagram of MnSc_2S_4 . Broken lines are phase boundaries determined by the neutron diffraction measurements²⁴. Filled circles and squares are the peaks and dips of κ_{xx} for field direction $\mathbf{B} \parallel [321]$, while crosses are those for $\mathbf{B} \parallel [111]$. (d) Field dependence of thermal conductivity κ_{xx} normalized by its value at $B = 0$ T at $T \leq 2$ K. The arrows indicate the positions of peaks and dips, plotted in panel (c). (e) Field dependence of κ_{xy}/T in the magnetically ordered phases. The shaded area represents the AFM-SkL phase^{24,25}. All the data points in κ_{xy}/T are the ones averaged over the field-up and field-down measurements, and the error bars are the maximum deviations of the data from the averages.

netic skyrmion lattice (AFM-SkL) realized in MnSc_2S_4 . By performing a large-scale period spin-wave theory, we show that the carriers are the magnons in a complex $\text{SU}(3)$ gauge field originating from the significant three-sublattice structure of skyrmions.

The AFM-SkL is a new class of skyrmion, recently discovered in a spinel compound MnSc_2S_4 . As shown in Fig. 1(a), the Mn^{2+} ($S = 5/2$) ions form a diamond lattice^{29,30} and undergo three successive magnetic transitions in a zero field, starting at $T \leq T_N = 2.3$ K from a modulated collinear phase to an incommensurate phase and finally showing a helical magnetic long-range order below 1.6 K^{24,25}. Interestingly, the phases above T_N may not be a simple paramagnet but a classical spiral-spin liquid phase characterized by a highly degenerate manifold of states with a series of continuous wave numbers forming surface in the reciprocal space^{25,31}. When a magnetic field \mathbf{B} is applied along the $[100]$, $[110]$, and $[111]$ direc-

tions, the helical phase transforms to the triple- Q phase at around $B = 4$ –6 T. Combining the neutron scattering experiment and Monte Carlo simulation, the triple- Q state in $\mathbf{B} \parallel [111]$ is identified as an AFM-SkL phase, which consists of three sublattices approximately forming a 120° -types of antiferromagnetic order. The structure shown in Fig. 1(b) is a cross-section of the diamond lattice forming a triangular lattice and stacks in the $[111]$ -direction with six-fold periodicity (64 sites per triangular lattice layer, $N_c = 384$ sites per unit cell). Each sublattice forms a triangular SkL, which can be well-explained theoretically within the classical framework^{32–34}.

II. EXPERIMENTAL

A. Synthesis and measurements

Single crystals of MnSc_2S_4 were synthesized by the chemical vapor transport method. We call two crystals with the shape of a thin plate with $[321]$ plane as sample #1 and $[111]$ plane as sample #2. The thermal-transport measurements were performed by the steady method by using a variable temperature insert (VTI) for 2–60 K and a dilution refrigerator (DR) for 0.1–3 K. The heat current J_Q was applied along $[\bar{1}11]$ ($[2\bar{1}\bar{1}]$) and the magnetic field \mathbf{B} was applied along $[321]$ ($[111]$) for the sample #1 (#2). The detailed setup of the thermal transport measurements is shown in Appendix §.A. In the main text, we show the experimental data for the sample #1. We find that both samples show essentially the same field dependence (see section V in SM), indicating high reproducibility of our results, and also confirming that the two field directions yield the same magnetic phases.

B. Phase diagram

We performed thermal transport measurements on the single crystals of MnSc_2S_4 using the setup shown in Appendix §.A. The detailed analysis of the field, temperature, and sample dependences are presented in Appendix §.A 2–§.A 5. Figure 1(c) shows the B - T phase diagram of MnSc_2S_4 at low temperature. The data points indicate the location of peaks and dips in the field dependence of the thermal conductivity (κ_{xx}) for two different field directions, $B \parallel [321]$ and $B \parallel [111]$, shown in Fig. 1(d). They are not much sensitive to the field direction, and show good agreement with the phase boundaries of the AFM-SkL phase obtained previously by the neutron diffraction experiment for $\mathbf{B} \parallel [111]$ ²⁴. Although the temperature dependence of κ_{xx} does not show a clear anomaly at T_N (see Appendix Fig. 6), the field dependence has distinct upturn and downturn, which are more visible for lower temperatures and disappear at $T \gtrsim T_N$. The good correspondence of these features with the phase boundaries indicate that κ_{xx} is strongly influenced by the magnetic ordering.

C. Thermal Hall measurement

Figure 1(e) shows the field-dependence of thermal Hall conductivity κ_{xy}/T at $T \leq 1$ K for $\mathbf{B} \parallel [321]$ of MnSc_2S_4 . In the helical phase at $B \lesssim 4$ T, κ_{xy}/T is suppressed to nearly zero or slightly negative values, which, however, shows an abrupt and substantial increase in entering the AFM-SkL phase at around 4 T. Its amplitude is overall suppressed at the lowest temperature 0.2 K, which is usual for the thermal Hall conductivity that relies on thermally driven bosonic excitations. At above ~ 8 T,

where the previous theory predicts a fan phase, κ_{xy}/T becomes suppressed but remain positive and finite.

D. Examination of the thermal conductivity

In magnetic insulators, the carriers contributing to thermal transport can be phonons and magnons. Here, we clarify experimentally that κ_{xx} has indeed a substantial contribution from magnons (κ_{xx}^{mag}) on top of phonons (κ_{xx}^{ph}). Figure 2(a) shows the field dependence of κ_{xx} at $T > T_N$ to be compared with Fig. 1(d) at $T \leq T_N$. The positive magnetothermal conductivity observed at lower fields for $T < T_N$ becomes negative above T_N .

The major effect of the magnetic field on the present system is to vary the magnon gap. In our theoretical calculation, when the system remains within the same phase the overall shape of the magnon bands does not change much while both the bandwidth and the gap vary (see Appendix Fig. 10). As shown in Fig. 3(e), the magnon gap first decreases toward zero in approaching the helical-to-AFM-SkL phase transition point slightly below 4 T, then increases again on entering the AFM-SkL phase, and closes at another transition point near 7 T. In general, an increase of magnon gap increases κ_{xx}^{mag} since the number of excited magnons that depends on the Bose distribution function increases. This can in turn suppress κ_{xx}^{ph} , supposing that there is a sufficiently large amount of scattering of phonons by the magnons.

For this reason, the positive magnetothermal conductivity observed at $T < T_N$ in decreasing the gap inside the helical phase is the feature attributed to an increase of κ_{xx}^{mag} . In the AFM-SkL phase, κ_{xx} shows a slight decrease, which should be because of the re-opening of the magnon gap in addition to a decrease of κ_{xx}^{ph} by the extra scattering effect of phonons by magnetic skyrmions as suggested in the case of ferro-SkL in GaV_4Se_8 ²².

In our experiment at $T = 3$ –8 K, there is a negative magnetothermal conductivity observed up to 8 T (Fig. 2(a)), which should be of magnon origin. It is known that a negative magnetothermal conductivity of κ_{xx}^{ph} is caused by a resonance scattering of phonons with spins³⁵. In that case, its field dependence scales with B/T , taking the minimum value when the Zeeman energy matches the thermal energy scale, $B \sim 4k_B T$, at which the phonon distribution reaches the maximum. However, the field dependence of κ_{xx} clearly does not scale with B/T (Fig. 7 in Appendix). Therefore, we conclude that a magnetic excitation possibly related to the spiral spin liquid phase²⁵ would be the origin of the negative magnetothermal conductivity. We further mention that magnons are good quasi-particles known to have a long lifetime at low temperature^{36–38}, and they suffer resonance scattering with phonons only at high energies where the magnon branches cross the phonon ones. The positive magnetothermal conductivity at high fields is due to the enhancement of κ_{xx}^{ph} caused by the suppression of magnetic fluctuations by the magnetic field.

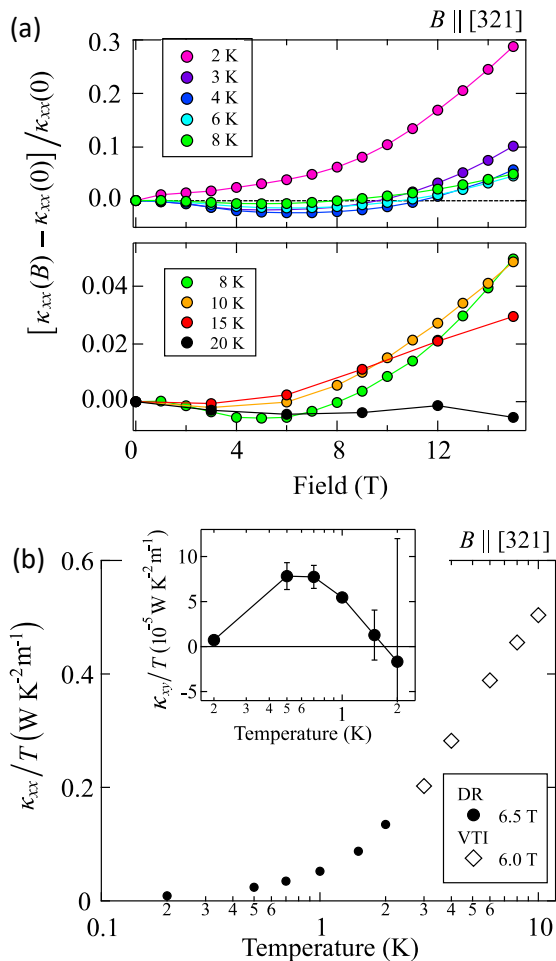


FIG. 2. (a) Field dependence of $\kappa_{xx}(B)$ normalized by the zero-field value above T_N . (b) Temperature dependence of κ_{xx}/T and κ_{xy}/T (inset) in the AFM-SkL phase (6.0 and 6.5 T) obtained by the DR (< 3 K) and the VTI (> 3 K) measurements.

We finally note that phonons are unlikely the origin of the thermal Hall effect, although κ_{xx}^{ph} is substantial in the AFM-SkL phase. For a thermal Hall effect of phonons, the temperature dependence of κ_{xy} is known to scale with that of κ_{xx} as observed in several materials^{39–41}. It is clearly not the case for MnSc_2S_4 as shown in Fig. 2(b); whereas κ_{xx}/T monotonically decreases as lowering T , κ_{xy}/T shows a peak at around $T_N/2$. This supports the magnon origin for the thermal Hall effect in the AFM-SkL phase.

III. THEORETICAL

A. model

We adopt the microscopic lattice model proposed in earlier work, that reproduces well the experimental observations in MnSc_2S_4 in their Monte Carlo simulation²⁴.

The Hamiltonian is given as

$$\mathcal{H} = \sum_{\mathbf{r}, \delta_l} \frac{J_l}{2} \mathbf{S}_{\mathbf{r}} \cdot \mathbf{S}_{\mathbf{r}+\delta_l} + \frac{3}{2} J_{\parallel} \sum_{\mathbf{r}, \delta_1} (\mathbf{S}_{\mathbf{r}} \cdot \hat{\delta}_1)(\mathbf{S}_{\mathbf{r}+\delta_1} \cdot \hat{\delta}_1) + A_4 \sum_{\mathbf{r}, \mu=x,y,z} (S_{\mathbf{r}}^{\mu})^4 - g\mu_B \sum_{\mathbf{r}} \mathbf{B} \cdot \mathbf{S}_{\mathbf{r}}. \quad (1)$$

Here, $S = 5/2$ and $(J_1, J_2, J_3) = (-0.31, 0.46, 0.087)$ K are the Heisenberg exchange interactions and δ_l ($l = 1, 2, 3$) are the corresponding vectors representing the first, second, and third neighbors in the diamond lattice ($\hat{\delta}_l$ is the unit vector). The anisotropic coupling constants are set to $J_{\parallel} = 0.01$ K and $A_4 = 0.0016$ K (in unit of temperature)²⁴. The details of the lattices parameters are shown in Appendix §.B 1.

We adopted the magnetic structures of the helical, fan, and AFM-SkL phases given in Appendix Eqs.(B2,B3). The magnetic periods are fixed whereas the amplitude of uniform magnetic moment M is determined to minimize the summation of classical (E_{cl}) and quantum zero-point fluctuation energy (E_{qc}).

B. Large-scale spin wave theory

Unlike the standard insulating ferro or antiferromagnets, whether and when the thermal Hall conductivity becomes finite in SkL is not well understood. The spin-wave theory for Néel type (ferro)-SkL on a triangular lattice is performed for a model with Heisenberg and DM interactions and single-ion uniaxial anisotropy^{42–44}, while they did not consider the transport properties. The thermal Hall effect observed in the ferromagnetic Néel SkL in GaV_4Se_8 is studied by the phenomenological U(1) gauge theory, showing a good agreement with the experimental data²². However, their Chern number and the Berry curvature contradict those of the spin-wave theory. Indeed, the Berry curvature depends much on the details of the Hamiltonian and the inter-band transition, and accordingly, the same SkL structure does not necessarily yield the same Berry curvature. In such a case, the simplest U(1) gauge theory may not be sufficient.

Therefore, taking advantages about the knowledge of Eq.(1) we performed a spin-wave theory for parameters where the magnetic orderings of large spatial periods take place, given as Eqs.(B2) and (B3). We perform a local gauge transformation to rotate the local spins to z -direction, and apply a Holstein-Primakoff transformation⁴⁵ in the rotating frame, solving the resultant large-scale spin-wave Hamiltonian represented by the $2N_s \times 2N_s$ matrix, where we take $N_s = 16$ for the helical phase and $N_s = 384$ for the AFM-SkL phase⁴⁶. For more details of the results, see Appendix §.B 2.

The magnon dispersions in an applied field are shown in Figs. 3(a) and 3(b) for the helical and fan phases and for AFM-SkL phases in Figs. 3(c) and 3(d) for two different field directions. The n -th magnon bands are colored by the density of Berry curvature $\Omega_{xy}^{(n)}$ they carry.

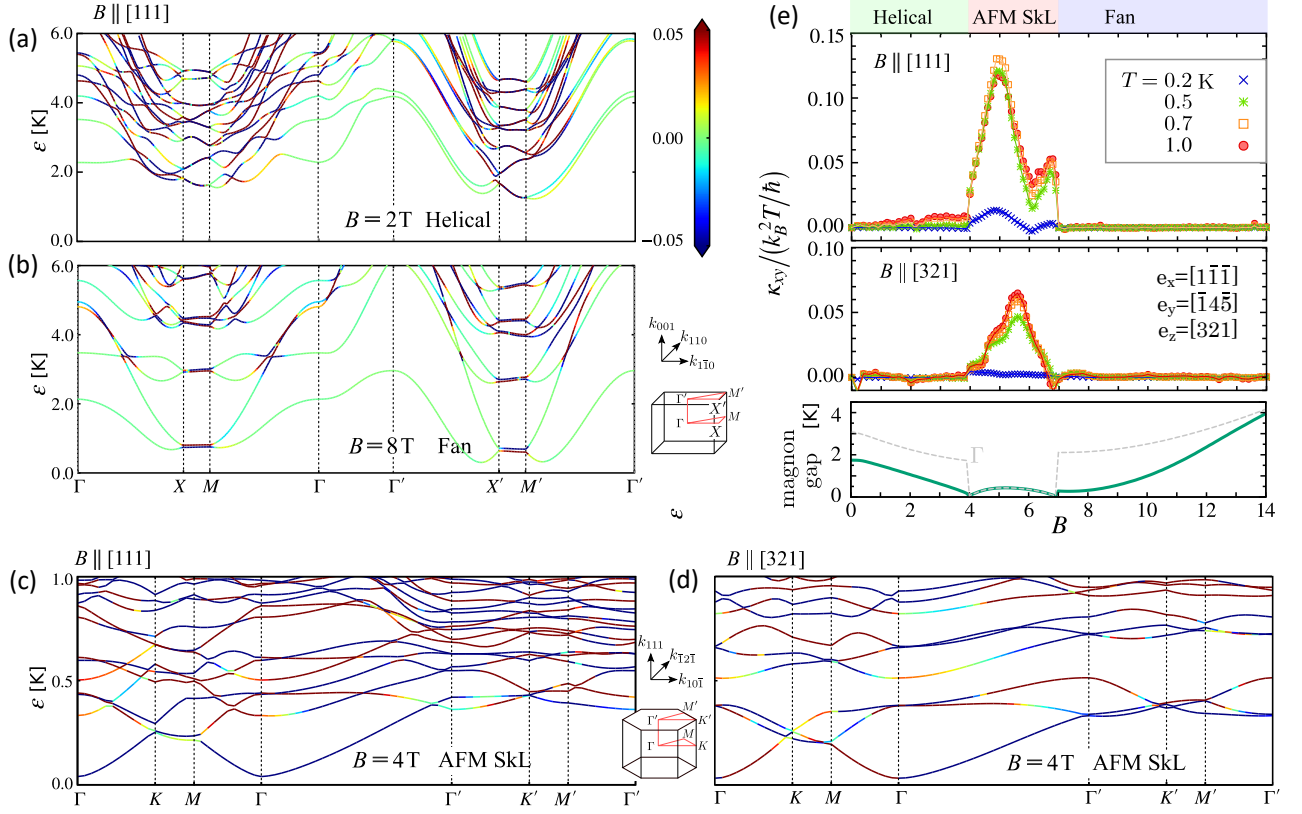


FIG. 3. (a-d) Magnon bands obtained by the spin-wave theory for the helical phase at $B = 2$ T ($N_c = 16$ site unit cell, $\mathbf{B} \parallel [111]$), the fan phase at $B = 8$ T ($N_c = 16$, $\mathbf{B} \parallel [111]$), and the AFM-SkL phase at $B = 4$ T ($N_c = 384$, $\mathbf{B} \parallel [111]$ and $[321]$). Reciprocal space is shown in the inset. Energy bands are shown with the color density plot of the Berry curvature $\Omega_{xy}^{(n)}$ at each \mathbf{k} -point. (e) Field dependent κ_{xy}/T for $T = 0.2, 0.5, 0.7, 1$ K from the linear-spin-wave theory using the same condition as panels (a)–(d). Field direction is taken as $\mathbf{B} \parallel [111]$ and $[321]$. The bottom panel shows the magnon gap (solid line) and the gap at Γ -point (broken line).

The thermal Hall conductivity is evaluated by integrating $\Omega_{xy}^{(n)}$ as⁴⁷,

$$\kappa_{xy} = -\frac{k_B^2 T}{\hbar} \int_{\text{BZ}} \frac{d^3 \mathbf{k}}{(2\pi)^3} \sum_{n=1}^{N_s} c_2[f(\varepsilon_n(\mathbf{k}))] \Omega_{xy}^{(n)}(\mathbf{k}), \quad (2)$$

where $f(\varepsilon) = 1/\{\exp(\varepsilon/k_B T) - 1\}$ is the Bose distribution function, and $c_2[x] = \int_0^x dt [\ln\{(1+t)/t\}]^2$.

The calculated field-dependence of κ_{xy} is shown in Fig. 3(e). It remains small in the helical phase, reflecting the observation in Fig. 3(a) that $\Omega_{xy}^{(n)}$ has finite contributions on part of the energy bands, while they are both positive and negative on nearby branches which mostly cancel out. If we perform the calculation by setting $J_{\parallel} = 0$, this small contribution disappears and $\kappa_{xy} = 0$ is obtained. This is because the anisotropic bond-dependent exchange interactions are the source of the Berry curvature⁴⁸.

Contrastingly, for AFM-SkL phase, $\Omega_{xy}^{(n)}$ takes overall large values throughout the whole energy bands, particularly, a large negative value on the lowest branch when $\mathbf{B} \parallel [111]$. This explains why κ_{xy} abruptly increases in

entering the AFM-SkL phase. In further increasing the field, κ_{xy} show peaks at 5 and 7 T for $\mathbf{B} \parallel [111]$ and at around 5.5 T for $\mathbf{B} \parallel [321]$. The field $\mathbf{B} \parallel [111]$ is perpendicular to the SkL plane and has a larger effect than $\mathbf{B} \parallel [321]$; the energy bands at $\varepsilon \gtrsim 0.5$ K are much dense and κ_{xy} are larger.

In the fan phase above 7 T, κ_{xy} almost disappears, since $\Omega_{xy}^{(n)}$ (see Fig. 3(b)) is mostly small except near the zone boundary. This does not explain a finite, almost field-independent κ_{xy} in the experiment. It should be noted that the energy scale of $B \gtrsim 8$ T is comparable to or higher than the temperature at which the classical spiral-spin liquid phase appears at zero-field characterized by the coexistent magnetic correlations of several different periods²⁵. This competition may transform the system into slightly different types of orderings or another liquid state. Namely, the state may not be the fan phase, which is beyond the description of Eq.(1). Apart from this issue, the consistency of theory and experiment at $B \lesssim 8$ T is sufficient to confirm that AFM-SkL phase yields substantial and stable $\kappa_{xy} > 0$.

C. SU(3) gauge theory

As mentioned earlier, a field-theoretical approach does not provide us with the quantitative understanding on the wave functions and related physical properties. Still, it may give a qualitative and intuitive understanding on how the magnons acquire their topological nature. In ferromagnets, the effect of DM interactions or the non-coplanar magnetic orderings were straightforwardly described by the U(1) gauge that served as a vector potential for magnons. In a similar context, the effect of magnetic texture of ferro-SkL is approximated as the U(1) gauge^{23,49}. Let us give an overview; the effect of slowly varying magnetic moments of ferro-SkL is naturally expressed by a single field operator $\hat{\mathbf{s}}(\mathbf{r})$, and the standard Heisenberg Hamiltonian on a discrete regular triangular lattice with lattice spacing a is converted by taking the continuum limit, $\hat{\mathbf{S}}_i \rightarrow \nu \hat{\mathbf{s}}(\mathbf{r})$ with unit cell volume $\nu = \sqrt{3}a^2/2$;

$$\mathcal{H}_{\text{eff}}^{\text{FM}} \sim 3J\nu \int d^2\mathbf{r} \hat{\mathbf{s}}^\dagger(\mathbf{r}) \left(1 + \frac{a^2}{4} \nabla^2\right) \hat{\mathbf{s}}(\mathbf{r}). \quad (3)$$

The Holstein-Primakoff transformation to the field operator is given as

$$\hat{\mathbf{s}}(\mathbf{r}) \sim \sqrt{\frac{S}{2\nu}} \left((b_{\mathbf{r}} + b_{\mathbf{r}}^\dagger) \mathbf{e}^x(\mathbf{r}) - i(b_{\mathbf{r}} - b_{\mathbf{r}}^\dagger) \mathbf{e}^y(\mathbf{r}) \right) + \left(\frac{S}{\nu} - b_{\mathbf{r}}^\dagger b_{\mathbf{r}} \right) \mathbf{e}^z(\mathbf{r}), \quad (4)$$

where the unit vectors $\mathbf{e}^\mu(\mathbf{r})$ ($\mu = x, y, z$) form a *local* orthogonal coordinate, with $\mathbf{e}^z(\mathbf{r}) \equiv \mathbf{m}(\mathbf{r})$ pointing in the direction of the ordered local moment specified by the angles $(\theta(\mathbf{r}), \phi(\mathbf{r}))$ (see Fig. 4(a)). Substituting Eq.(4) to Eq.(3) and by keeping derivative of \mathbf{e}^μ up to the first order, we obtain

$$\mathcal{H}_{\text{eff}}^{\text{FM}} \sim 6J\nu \int d^2\mathbf{r} b_{\mathbf{r}}^\dagger (\nabla - i\mathbf{A}(\mathbf{r}))^2 b_{\mathbf{r}}, \quad (5)$$

where $\mathbf{A}(\mathbf{r}) = -\cos\theta(\mathbf{r})\nabla\phi(\mathbf{r})$ serves as a fictitious U(1) vector potential and is generated by the spatial variation of angles θ and ϕ (see Fig. 4(b)). When we put it back to the bosons b_i on lattice sites, we obtain $\mathcal{H}_{\text{eff}}^{\text{FM}} \sim JS \sum_{i,j} U_{ij} b_i^\dagger b_j$ with the U(1) gauge given as $U_{ij} = \exp(i \int_{\mathbf{r}_i}^{\mathbf{r}_j} d\mathbf{r} \cdot \mathbf{A}(\mathbf{r}))$.

In the present AFM-SkL, three sublattices equivalently form a large-scale SkL structure. This requires at least three field operators $\hat{\mathbf{s}}_\ell(\mathbf{r})$ ($\ell = A, B, C$) that describe the spatial variation of moments of the three sublattices (Figs. 4(c),(d)). The Heisenberg Hamiltonian is given by the coupling between them as

$$\mathcal{H}_{\text{eff}}^{\text{AFM}} \sim \frac{J\nu}{2} \int d^2\mathbf{r} \sum_{\ell,\ell'} \hat{\mathbf{s}}_\ell^\dagger(\mathbf{r}) \left(1 + \frac{a^2}{4} \nabla^2\right) \hat{\mathbf{s}}_{\ell'}(\mathbf{r}). \quad (6)$$

Here, we discard the magnetic anisotropy terms of Eq.(1) which does not deteriorate the following discussions. Introducing three species of Holstein-Primakoff bosons

$b_\ell(\mathbf{r})$ by adding indices $\ell = A, B, C$ to Eq.(4), we reach the following effective Hamiltonian for the AFM-SkL,

$$\mathcal{H}_{\text{eff}}^{\text{AFM}} \sim \int d^2\mathbf{r} \Phi^\dagger(\mathbf{r}) \left[\mathbf{F}(\mathbf{r}) a^2 \nabla^2 + \sum_{\mu=x,y} \mathbf{G}_\mu(\mathbf{r}) a \partial_\mu \right] \Phi(\mathbf{r}),$$

where $\Phi^\dagger(\mathbf{r}) = (b_A^\dagger, b_B^\dagger, b_C^\dagger)$ and $\mathbf{F}(\mathbf{r})$ and $\mathbf{G}_\mu(\mathbf{r})$ are 6×6 matrices consisting of \mathbf{e}_ℓ^μ and $\mathbf{e}_{\ell'}^\mu$ and $\mathbf{e}_\ell^\mu \cdot \partial_\mu \mathbf{e}_{\ell'}^\mu$, respectively, with $\ell \neq \ell'$. In particular, the diagonal elements of $\mathbf{G}_\mu(\mathbf{r})$ are proportional to the U(1) gauge fields of the three sublattices, $\mathbf{A}_\ell(\mathbf{r}) = -\cos\theta_\ell(\mathbf{r})\partial_\mu\phi_\ell(\mathbf{r})$. We show in Fig. 4(e) the profiles of $\mathbf{A}_\ell(\mathbf{r})$ calculated as continuous two-dimensional vector fields and the corresponding fictitious fields are given as

$$b_\ell^z(\mathbf{r}) = \partial_x A_\ell^y(\mathbf{r}) - \partial_y A_\ell^x(\mathbf{r}) \quad (8)$$

(see Appendix §.B.4 for details). We see that the locations where $\mathbf{m}(\mathbf{r})$ points in the z -direction ($\theta = 0, \pi$) serve as vortex centers of $\mathbf{A}_\ell(\mathbf{r})$ and generate large $b_\ell^z(\mathbf{r})$.

However, there are substantial off-diagonal elements in $\mathbf{G}_\mu(\mathbf{r})$ that couple these three U(1) gauge fields and transform them to the SU(3) gauge fields. Let $\Psi^\dagger(\mathbf{r})$ be the operators obtained by the unitary transformation to $\Phi^\dagger(\mathbf{r})$ that diagonalizes $\mathbf{F}(\mathbf{r})$, where we find the form

$$\hat{\mathcal{H}}_{\text{eff}}^{\text{AFM}} \sim \int d^2\mathbf{r} \Psi^\dagger(\mathbf{r}) \left[\sum_{\mu=x,y} (I_{3 \times 3} \partial_\mu + \mathbf{T}_\mu(\mathbf{r}))^2 \otimes \tau^x \right] \Psi(\mathbf{r}), \quad (9)$$

where $\mathbf{G}_\mu(\mathbf{r})$ is converted to the 3×3 matrix $\mathbf{T}_\mu(\mathbf{r})$ that serves as a high-rank vector potential for the SU(3) gauge field, as we find from the analogy with Eq.(5).

IV. SUMMARY AND DISCUSSION

We have experimentally measured the thermal conductivity κ_{xx} and thermal Hall conductivity κ_{xy}/T of the insulating magnet MnSc₂S₄ in an applied field up to 14 T and found a substantial thermal Hall effect that emerges in the AFM-SkL phase in an applied field of $B \sim 4\text{--}8$ T at temperatures $T \lesssim 1$ K lower than T_N . By performing a large-scale spin wave theory considering the Hamiltonian specific to the material, we showed that the AFM-SkL exhibits a very dense magnon band structure, and hosting a large amount of Berry curvature. The corresponding thermal Hall coefficient calculated from Helical to AFM-SkL phases in increasing the magnetic field consistently explains the experimental observations.

We now discuss in more detail the correspondence of the experiment in Fig. 1(e) and the theory in Fig. 3(e) for $\mathbf{B} \parallel [321]$. Although we cannot precisely refer to the small structures in the experimental data that may depend on sample qualities, the common features are captured very well; at 0.2 K, κ_{xy} remains small and structureless, while for 0.5, 0.7, and 1 K, there is a single peak at around 5.5–6 T and the amplitudes no longer differ much for different temperatures. To understand these features, we calculate how many magnon bands from the bottom would

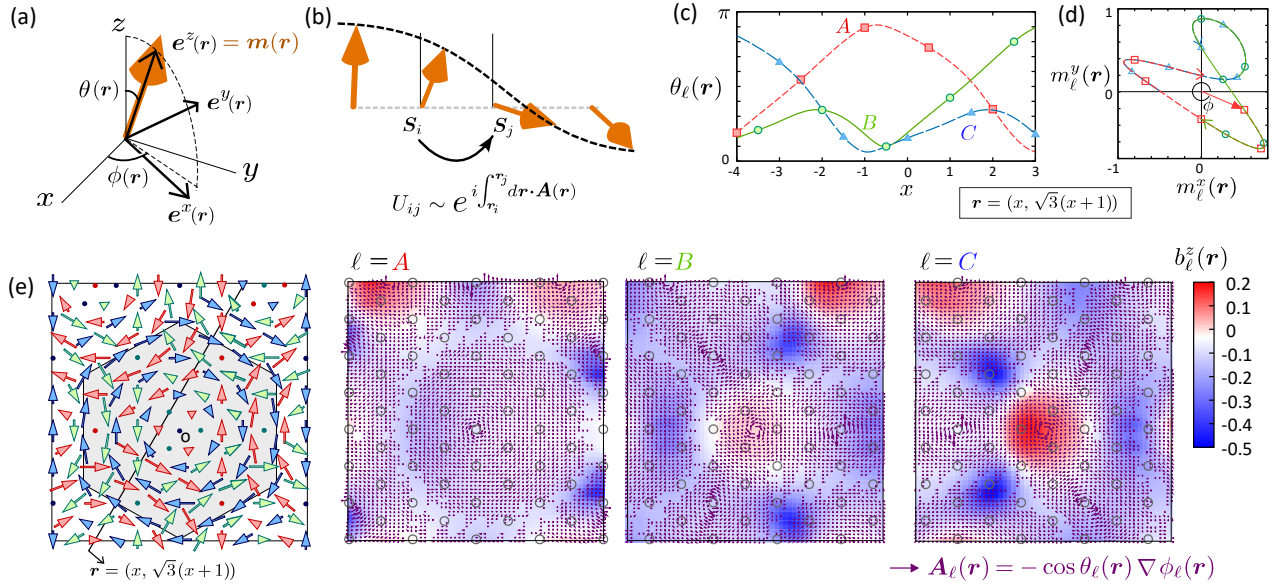


FIG. 4. (a,b) Schematic description of the ordered spin moments slowly varying in space. The x, y, z -component of spin $\mathbf{S}(\mathbf{r})$ point toward $(\mathbf{e}^x(\mathbf{r}), \mathbf{e}^y(\mathbf{r}), \mathbf{e}^z(\mathbf{r}))$ which form the local coordinate with $\mathbf{e}^z(\mathbf{r}) = \mathbf{m}(\mathbf{r})$ specified by the angle $(\theta(\mathbf{r}), \phi(\mathbf{r}))$. (c,d) $\theta_\ell(\mathbf{r})$ and $m_\ell^y(\mathbf{r})$ versus $m_\ell^x(\mathbf{r})$ along the line, $\mathbf{r} = (x, \sqrt{3}(x+1))$, shown in panel **d**, whose tangent give the angle ϕ_ℓ . (e) The right three panels show the detailed information of the U(1) gauge field based on the independent three sublattices; $\mathbf{A}_\ell(\mathbf{r}) = -\cos \theta_\ell(\mathbf{r}) \nabla \phi_\ell(\mathbf{r})$ as arrows and $b_\ell^z(\mathbf{r})$ as density plot. Small circles indicate the location of sublattice sites. Left panel is the corresponding AFM-SkL structure on the triangular lattice colored red, green and blue for $\ell = A, B, C$ sublattices, respectively.

give major contributions to κ_{xy} (Appendix Fig. 11). At 0.2 K, including 24 bands already reproduces well the results of the full 384 bands, while at 0.5 K, the 24 bands corresponding to the energy window of up to 2 K are not at all sufficient. This means that the dense band structure of skyrmions including those at high energies plays a crucial role in magnon transport. Therefore, although the magnon gap increases toward 5 T and then decreases with a field, κ_{xy} is not sensitive to this gap opening. The nontrivial distribution of $\Omega_{xy}^{(n)}$ up to the high energy determines the field dependence of κ_{xy} .

In this context, one needs to be careful about the Chern numbers or equivalently the Berry curvatures that depend on the details of the Hamiltonian. Even for the simple ferromagnetic Néel SkL phase of GaV_4Se_8 ²², although the phenomenological U(1) gauge theory give κ_{xy} in good agreement with the experimental data, the corresponding Chern number contradicts those obtained by the spin-wave theory^{43,50} at the lowest two energy bands. The values of κ_{xy} that have contributions of Berry curvature from a wide range of bands are particularly sensitive to the details and need an accurate treatment for their quantitative evaluation.

However, an overall origin of the emergent Berry curvature of magnon bands in the AFM-SkL is the SU(3) gauge as we discussed earlier. To give an intuitive understanding, it is useful to refer to the antiferromagnets on bipartite lattices, where the two species of magnons on the two sublattices can be regarded as up and down

pseudo-spin ones. When the antisymmetric or spatially anisotropic exchange couplings are introduced, they serve as “pseudo-spin-orbit coupling”, which mixes the motion of up and down magnons^{26–28}. This effect is represented by the SU(2) gauge field on magnons in analogy with the SU(2) hopping of Rashba electrons of semiconductors⁵¹, and allowed the thermal Hall effect on a square lattice antiferromagnet²⁷ which was prohibited in the U(1) picture¹⁹.

In the present triangular-based system, we have three types of magnons living on the three sublattices, which can be regarded as three-component pseudo-spins. If the magnetic moments form a regular coplanar 120° ordering, we find $\mathbf{G}_\mu(\mathbf{r}) = 0$, namely we do not have the spatial variation of $\hat{s}_\ell(\mathbf{r})$ for the U(1) gauge field. In the AFM-SkL phase, the U(1) gauge fields are switched on, and at the same time they communicate with each other through the “pseudo-spin-orbit coupling” given by the off-diagonal $\mathbf{G}_\mu(\mathbf{r})$ that originate from the exchange interactions between spins on different sublattices. The SU(3) pseudo-spin represents the sublattice degrees of freedom and the “orbit” refers to the kinetic motions of magnons.

The SU(3) gauge has been a theoretical object for describing the interactions of quarks or gluons in particle physics, and not much has been discussed in condensed matter, particularly in experiment. While the SU(3) symmetry can sometimes appear, e.g. in cold atoms⁵² and the SU(3) Heisenberg Hamiltonian may yield exotic

phases⁵³, the present system would be the first to observe experimentally the phenomena that directly reflect the SU(3) gauges in material solids.

ACKNOWLEDGMENTS

The work is supported by JSPS KAKENHI Grants No. JP19H01848, No. JP17K05533, No. JP18H01173, No. 20K03773, No. JP21H05191, No. JP21K03440, No. 21H01035, and No. 17H06137 from the Ministry of Education, Science, Sports and Culture of Japan and the Murata Science Foundation.

Appendix A: Details of the thermal transport measurements

We show the measurement setup, the magnetic field dependence of κ_{xx} , the field-injection process dependence of κ_{xy} , and the sample dependences of both of them.

1. Measurement setup

As shown in Figs. 5(a) and 5(b), one heater and three thermometers (T_{High} , T_{L1} , and T_{L2}) were attached to the sample using a silver paste. The sample size is about $1.0 \times 0.8 \times 0.07 \text{ mm}^3$. To avoid a background signal coming from metal, the sample was attached to the insulating LiF heat bath with non-metallic grease. The heat current J_Q and the magnetic field B were applied along [111] and [321] directions of the sample, respectively. Both the longitudinal ΔT_x ($\Delta T_x = T_{\text{High}} - T_{L2}$) and the transverse ΔT_y ($\Delta T_y = T_{L1} - T_{L2}$) temperature differences were measured as a function of the heat current $J_Q = Q/wt$, where Q is the heater power, t is the thickness of the sample, and w is the mean sample width. To cancel the longitudinal component in ΔT_y by the misalignment effect, ΔT_y was asymmetrized with respect to the field direction as $\Delta T_y^{\text{asym}} = \Delta T_y(+B) - \Delta T_y(-B)$. To take into account a magnetic hysteresis effect, this antisymmetrization was done separately for the data obtained in the field-up process and that in the field-down process. The thermal (Hall) conductivity κ_{xx} (κ_{xy}) is derived by

$$\begin{pmatrix} Q/wt \\ 0 \end{pmatrix} = \begin{pmatrix} \kappa_{xx} & \kappa_{xy} \\ -\kappa_{xy} & \kappa_{xx} \end{pmatrix} \begin{pmatrix} \Delta T_x/L \\ \Delta T_y^{\text{asym}}/w' \end{pmatrix}, \quad (\text{A1})$$

where L is the length between the thermal contacts for reading T_{High} and T_{L1} and w' is the length between the thermal contacts for T_{L1} and T_{L2} . The irregular shape of the sample and the finite size of the thermal contacts

cause uncertainty in estimating these geometrical factors, resulting in the ambiguity of the absolute values of κ_{xx} and κ_{xy} by a factor of 2–4.

2. Estimation of the phonon mean free path

Figure 6(a) shows the temperature dependence of κ_{xx} in a zero external magnetic field. It exhibits a T^2 behavior without a clear anomaly at the Néel temperature ($T_N = 2.3 \text{ K}$). Here, we estimate the phonon mean free path (ℓ_{mfp}) by assuming that κ_{xx} is only given by phonons (κ_{xx}^{ph}) as shown in Fig. 6(b).

The process of evaluating ℓ_{mfp} is given as follows. The thermal conductivity of phonons is given by

$$\kappa_{xx}^{\text{ph}} = \frac{1}{3} C_{\text{ph}} v_{\text{ph}} l_{\text{ph}}, \quad (\text{A2})$$

where C_{ph} , v_{ph} , and l_{ph} are the heat capacity, the sound velocity, and the mean free path of phonons, respectively. Referring to Ref.[29], we obtain the temperature dependence of C_{ph} for acoustic phonons. The sound velocity is estimated as approximately 1770 m/s from the Debye temperature of 154 K.

3. Magnetic field dependence of κ_{xx}

Figure 7(a) shows B -dependence of $\kappa_{xx}(B)$ normalized as $(\kappa_{xx}(B) - \kappa_{xx}(0))/\kappa_{xx}(0)$ in the temperature range of 3 K

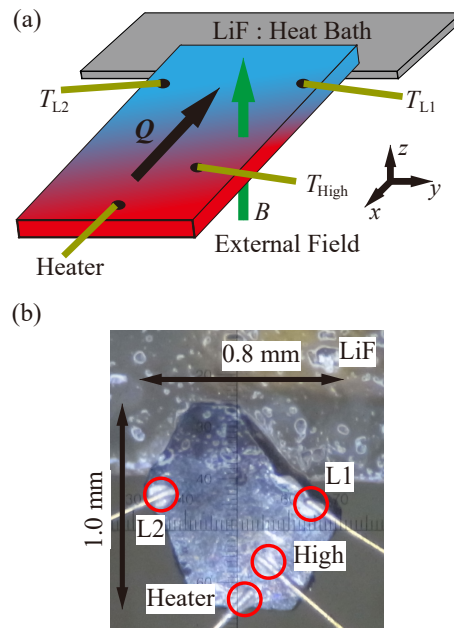


FIG. 5. (a) Schematic figure of the setup of the thermal transport measurements. (b) Photograph of the sample mounted on the heat bath of LiF. The thermal contacts for the heater and the thermometers are marked by red circles.

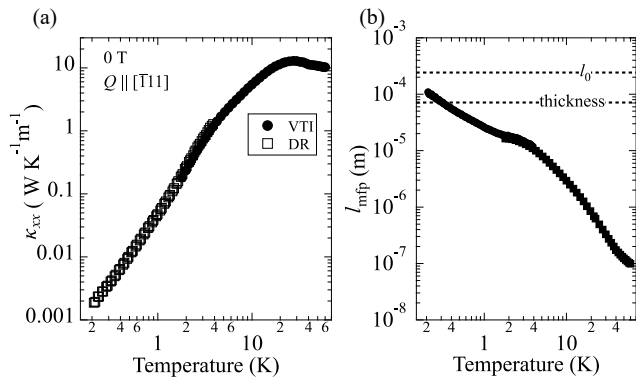


FIG. 6. (a) Temperature dependence of κ_{xx} at zero external field measured in the variable-temperature insert (VTI, circles) and the dilution refrigerator (DR, squares). (b) Phonon mean free path estimated by assuming that the data in panel (a) is solely from phonons.

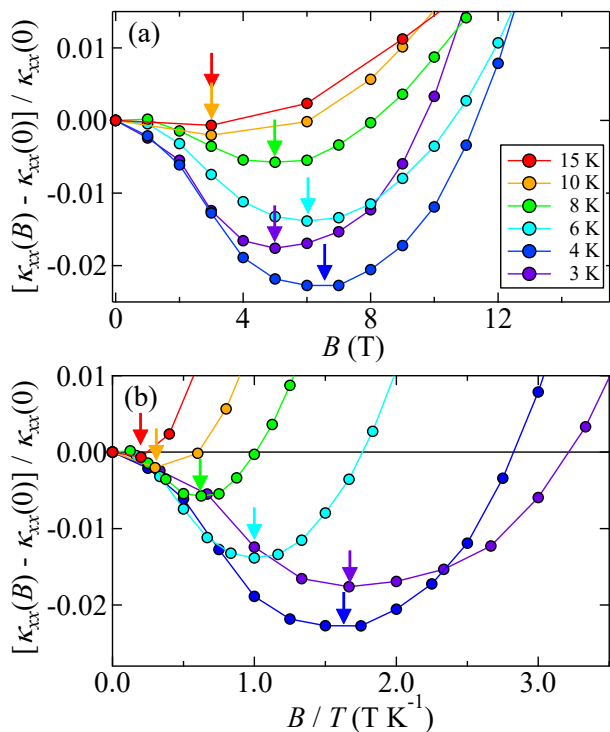


FIG. 7. Normalized κ_{xx} as a function of (a) B and (b) B/T for several choices of temperatures above T_N . Arrows denote the minimum position of normalized κ_{xx} .

$\leq T \leq 15$ K. The field at which the normalized $\kappa_{xx}(B)$ takes the minimum shifts to higher fields when lowering the temperature from 15 K to 4 K, and then slightly shifts to the lower field at 3 K. The suppression of κ_{xx} by the magnetic field (negative magneto thermal conductivity) can be attributed to the decrease of either κ_{ph} or κ_{mag} .

The former suppression originates from the resonance scattering effect of phonons due to spins, and should be enhanced the most when the energy scale $4k_B T$ that gives

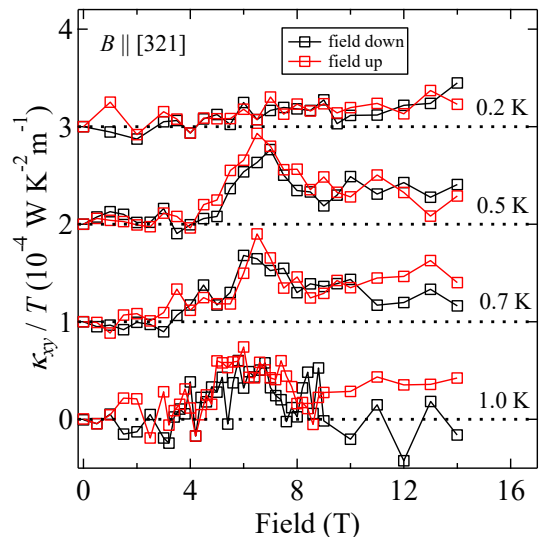


FIG. 8. Magnetic field B dependence of κ_{xy}/T obtained in the field up and down processes for sample #1.

the maximum of the density distribution of phonons becomes equal to the Zeeman splitting, $gS\mu_B B$. We plotted the normalized κ_{xx} as a function of B/T in Fig. 7(b). If this scenario applies, κ_{xx} should take the minimum at $B/T \sim 4k_B/gS\mu_B$, independent of T , which does not happen here. Therefore, we conclude that the suppression of κ_{xx}^{ph} by the magnetic field is not ascribed to the resonant scattering effect of phonons.

The remaining possibility is the decrease of κ_{xx}^{mag} . Since the Weiss temperature is -23 K, the antiferromagnetic correlation will develop at temperatures below 20 K. In fact, the magnetic specific heat is found to increase with decreasing temperature at $T < 15$ K. In frustrated insulating quantum magnets, such strong spin correlation, even though they may not form a long-range order, is known to sometimes host a spinons excitation that carries heat current. In MnSc_2S_4 , in a paramagnetic phase at low temperatures above T_N is possibly a classical spiral-spin liquid. There, the magnetic diffuse scattering experiments show the existence of some sort of magnetic excitations relevant to a manifold of wave numbers forming surfaces in the reciprocal space, characterizing this classical spin liquid. Therefore, it is natural to consider that the external magnetic field will suppress the strong fluctuation of this spiral spin liquid and decreases κ_{xx}^{mag} accordingly. This scenario is consistent with the observed energy scales: the order of the magnetic interaction ~ 20 K and the location of minimum ~ 6 T.

4. Field-up and down processes of κ_{xy}/T

Since magnetic skyrmions are a metastable magnetic order that can not appear without the aid of a magnetic field or strong magnetic anisotropy, it is often found in the previous studies^{22,54-58} that the phase boundary

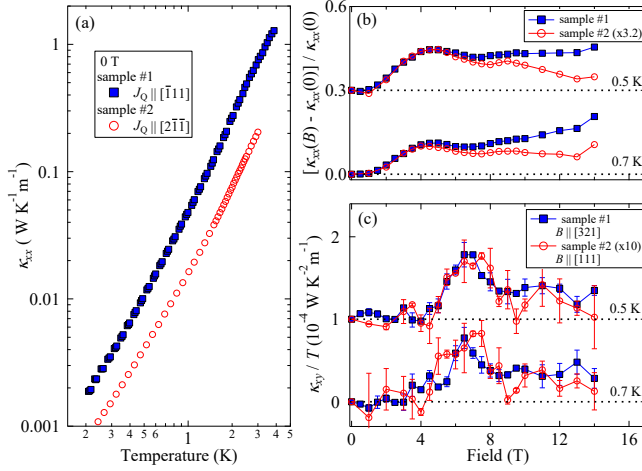


FIG. 9. (a) Temperature dependence of κ_{xx} for sample #1 and sample #2. Field B dependence of (b) normalized κ_{xx} and (c) κ_{xy}/T at $T=0.5\text{K}$ and 0.7K obtained in the field up and down processes for the two samples.

(1st order phase transition) between SkL phase and the other phases usually vary, or the density of skyrmions may change according to the history of applying a magnetic field. The change in skyrmion density will vary the magnon density which easily influences the thermal transport. Therefore, we measured the thermal Hall conductivity for the field-up and field-down processes. Figure 8 shows κ_{xy}/T as a function of field-up and field-down for temperatures $T = 0.2, 0.5, 0.7,$ and 1K . We find that the two processes agree well, indicating that the phase boundaries do not depend on the processes. This behavior is in sharp contrast to the other skyrmion materials, e.g. GaV_4Se_8 , that exhibit different behavior between field-up and down processes. The data points given in Fig. 1(d) in the main text are the ones averaged for the two processes, and the error bars are the maximum deviation of the measured data from the average values.

5. Thermal transport properties of sample #2

The B - T phase diagram of MnSc_2S_4 are studied in detail for $\mathbf{B} \parallel [111]$ and $\mathbf{B} \parallel [110]$. Since for the former case, the phase boundary has a simple structure as a function of field, we studied sample #2 which has $[111]$ plane at the sample surface. Here, we compare the results of sample #2 with those of sample #1 shown in the main text.

Figure 9(a) shows the temperature dependence of κ_{xx} . Since the sample quality is not as good for sample #2 as sample #1, the absolute values differ by a factor of two, while they show good agreement in their temperature dependences.

As shown in Fig. 9(b), the value of κ_{xx} normalized by the zero-field values show very good agreement with those of sample #1 for $B < 9\text{T}$. The peak at around 4T

and the dips at 7T are the anomalies that take place at the magnetic phase transition points reported previously. For fields higher than 9T , the normalized κ_{xx} of sample #2 show strong suppression in further increasing B . This is in sharp contrast to the case of sample #1. Since the high-field phase for $\mathbf{B} \parallel [111]$ is the multi-domain phase consisting of single- Q state, the field angle may influence the structure of the domain and accordingly, the magnitude of orderings. Since thermal transport at low temperatures is very likely to be caused by magnons, the number of carriers may change due to this effect.

In Fig. 9(c) we show the κ_{xy}/T as function of B for 0.5K and 0.7K . Although the amplitude of κ_{xy}/T of sample #2 is about $1/10$ of that of sample #1, the profile of the field dependences after scaling the factor shows very good agreement. We thus expect that the magnetic phases show the same dependence on the field $\mathbf{B} \parallel [321]$ and $\mathbf{B} \parallel [111]$ below 9T , as has been confirmed in Figs. 9(a) and 9(b). It has been shown previously that the AFM-SkL phase appears not only in the particular field direction $\mathbf{B} \parallel [111]$ but also along $\mathbf{B} \parallel [100]$ and $\mathbf{B} \parallel [110]$, although the shapes of the phase boundaries differ³³. Therefore, we can safely conclude that the results we obtained for $\mathbf{B} \parallel [321]$ for sample #1 is the one that detects the emergent AFM-SkL phase reported previously.

Appendix B: Theoretical

1. Details of the spin wave theory

We consider the spin Hamiltonian on a diamond lattice in Eq.(1) in the main text. The vectors $\hat{\delta}_1, \hat{\delta}_2$ and $\hat{\delta}_3$ showing uniaxial spin anisotropy along the bond directions of the lattice is

$$\begin{aligned}
 4\hat{\delta}_1 &= (1, 1, 1), (-1, 1, 1), (1, -1, 1), (1, 1, -1), \\
 &\quad (-1, -1, 1), (1, -1, -1), (-1, 1, -1), (-1, -1, -1), \\
 2\hat{\delta}_2 &= (1, 0, 1), (0, 1, 1), (-1, 0, 1), (0, -1, 1), \\
 &\quad (1, 1, 0), (1, -1, 0), (-1, 1, 0), (-1, -1, 0), \\
 &\quad (1, 0, -1), (0, 1, -1), (-1, 0, -1), (0, -1, -1), \\
 4\hat{\delta}_3 &= (3, 1, 1), (-3, 1, 1), (3, -1, 1), (3, 1, -1), \\
 &\quad (-3, -1, 1), (3, -1, -1), (-3, 1, -1), (-3, -1, -1), \\
 &\quad (1, 3, 1), (-1, 3, 1), (1, -3, 1), (1, 3, -1), \\
 &\quad (-1, -3, 1), (1, -3, -1), (-1, 3, -1), (-1, -3, -1), \\
 &\quad (1, 1, 3), (-1, 1, 3), (1, -1, 3), (1, 1, -3), \\
 &\quad (-1, -1, 3), (1, -1, -3), (-1, 1, -3), (-1, -1, -3).
 \end{aligned} \tag{B1}$$

where we need to remove the ones not on the diamond lattice when implementing them into Eq.(1).

Helical and fan phases.

The normalized vector spins of the classical helical and

fan ground states are given by

$$\mathbf{m}_r \propto -\sin(\mathbf{q} \cdot \mathbf{r})\mathbf{e}_{1\bar{1}0} - \cos(\mathbf{q} \cdot \mathbf{r} + \phi)\mathbf{e}_{110} + M\mathbf{e}_h, \quad (\text{B2})$$

where $\phi = -\pi$ for the helical phase and $\phi = -3\pi/2$ for the fan phase, \mathbf{e}_{abc} is the unit vector along the [abc] direction, \mathbf{e}_h is the unit vector along the magnetic field \mathbf{h} , and $\mathbf{q} = \frac{3\pi}{2}(1, 1, 0)$. The primitive translation vectors are $\mathbf{a}_1 = (2, 2, 0)$, $\mathbf{a}_2 = (\frac{1}{2}, -\frac{1}{2}, 0)$, $\mathbf{a}_3 = (0, 0, 1)$, where there are 16 sites in the magnetic unit cell. The reciprocal lattice vectors are $\mathbf{b}_1 = \frac{\pi}{2}(1, 1, 0)$, $\mathbf{b}_2 = 2\pi(1, -1, 0)$, $\mathbf{b}_3 = 2\pi(0, 0, 1)$.

Antiferromagnetic skyrmion lattice phase.

The normalized vector spins of the classical AFM-SkL ground state is given by

$$\mathbf{m}_r \propto \sum_{m=1}^3 (\sin(\mathbf{q}_m \cdot \mathbf{r})\mathbf{e}_m - \cos(\mathbf{q}_m \cdot \mathbf{r} - 9\pi/8)\mathbf{e}_{111}) + M\mathbf{e}_h, \quad (\text{B3})$$

where $\mathbf{e}_l = \mathbf{e}_{1\bar{1}2}$, $\mathbf{e}_{1\bar{2}1}$, $\mathbf{e}_{2\bar{1}1}$. and $\mathbf{q}_1 = \frac{3\pi}{2}(1, -1, 0)$, $\mathbf{q}_2 = \frac{3\pi}{2}(1, 0, -1)$, $\mathbf{q}_3 = \frac{3\pi}{2}(0, 1, -1)$. There are 384 sites in the magnetic unit cell spanned by $\mathbf{a}_1 = (4, 0, -4)$, $\mathbf{a}_2 = (0, 4, -4)$, $\mathbf{a}_3 = (1, 1, 1)$. The reciprocal lattice vectors are given by $\mathbf{b}_1 = \frac{\pi}{6}(2, -1, -1)$, $\mathbf{b}_2 = \frac{\pi}{6}(-1, 2, -1)$, $\mathbf{b}_3 = \frac{2\pi}{3}(1, 1, 1)$.

Gauge transformation and spin wave Hamiltonian.

For the spin wave analysis, we first introduce the three-dimensional rotation matrix as

$$R_r^{\mu\nu} = n_r^\mu n_r^\nu + (\delta^{\mu\nu} - n_r^\mu n_r^\nu) \cos \phi_r - \sin \phi_r \sum_\rho \epsilon^{\mu\nu\rho} n_r^\rho, \quad (\text{B4})$$

where vector \mathbf{n}_r and angle ϕ_r are defined as

$$\mathbf{n}_r = \frac{\mathbf{m}_r \times \mathbf{e}^z}{|\mathbf{m}_r \times \mathbf{e}^z|}, \quad \phi_r = \arccos(\mathbf{e}^z \cdot \mathbf{m}_r). \quad (\text{B5})$$

This matrix satisfies $R_r \mathbf{m}_r = \mathbf{e}^z$, meaning that it rotates the direction of the spin to the quantization axis (z -axis), which is the local gauge transformation changing the representation of the Hamiltonian but not the physical quantities.

We apply the Holstein-Primakoff transformation in the rotating frame,

$$R_r \hat{\mathbf{S}}_r \simeq \sqrt{\frac{S}{2}}(\hat{b}_r + \hat{b}_r^\dagger)\mathbf{e}^x - i\sqrt{\frac{S}{2}}(\hat{b}_r - \hat{b}_r^\dagger)\mathbf{e}^y + (S - \hat{b}_r^\dagger \hat{b}_r)\mathbf{e}^z. \quad (\text{B6})$$

The spin Hamiltonian is approximated as $\hat{\mathcal{H}} \simeq E_{\text{cl.}} + \hat{\mathcal{H}}_{\text{mag.}}$, where the magnon Hamiltonian $\hat{\mathcal{H}}_{\text{mag.}}$ is calcu-

lated as

$$\hat{\mathcal{H}}_{\text{mag.}} = \sum_r \varepsilon_r \hat{b}_r^\dagger \hat{b}_r + \frac{1}{2} \sum_r \left(\lambda_r (\hat{b}_r^\dagger)^2 + \text{h.c.} \right) \quad (\text{B7})$$

$$+ \frac{1}{2} \sum_r \sum_m \sum_{\delta_m} \left(t_{r,\delta_m} \hat{b}_r^\dagger \hat{b}_{r+\delta_m} + \Delta_{r,\delta_m} \hat{b}_r^\dagger \hat{b}_{r+\delta_m}^\dagger X + \text{h.c.} \right). \quad (\text{B8})$$

We perform Fourier transformation $\hat{b}_r = \sqrt{N_s}^{-1} \sum_{\mathbf{k}} \hat{b}_{\mathbf{k},\alpha} e^{i\mathbf{k} \cdot \mathbf{r}}$, where $N_s = 16$ and 384 for helical/fan and AFM-SkL phases, and $\alpha = 1, 2, \dots, N_s$ is the sublattice site index within the magnetic unit cell.

The magnon Hamiltonian is rewritten as using $\hat{\Phi}_{\mathbf{k}} = (\hat{b}_{\mathbf{k},1}, \dots, \hat{b}_{\mathbf{k},N_s})$ as

$$\hat{\mathcal{H}}_{\text{mag.}} = \frac{1}{2} \sum_{\mathbf{k}} \hat{\Phi}_{\mathbf{k}}^\dagger H_{\text{BdG}}(\mathbf{k}) \hat{\Phi}_{\mathbf{k}} + \text{const.}, \quad (\text{B9})$$

$$H_{\text{BdG}}(\mathbf{k}) = \begin{pmatrix} \Xi(\mathbf{k}) & \Delta(\mathbf{k}) \\ \Delta^*(-\mathbf{k}) & \Xi^*(-\mathbf{k}) \end{pmatrix}, \quad (\text{B10})$$

The magnon bands and eigenstates can be obtained by solving the eigenvalue equations, $\Sigma^z H_{\text{BdG}}(\mathbf{k}) \mathbf{t}_n(\mathbf{k}) = \varepsilon_n(\mathbf{k}) \mathbf{t}_n(\mathbf{k})$, with $\Sigma^z = \sigma^z \otimes I_{N_s \times N_s}$. By using magnon eigenstates, $\mathbf{t}_n(\mathbf{k})$, we obtain the Berry curvature and the thermal Hall conductivity in the main text.

2. Variation of magnon bands

In Fig. 10(a) we show the magnon bands obtained at $B = 2$ T by artificially setting $J_{\parallel} = 0$, which gives the coplanar magnetic structure instead of the helical one. There, we find that although the band structures look similar to the one shown in Fig. 3(a) in the main text, they have mostly $\Omega_{xy}^n = 0$, indicating that the coplanar phase does not have room to exhibit a thermal Hall effect. This indicates that the anisotropic exchange interactions are essential to have a finite Berry curvature.

Figure 10(b) shows the magnon bands for AFM-SkL phase in higher fields. At 5 T, we find a much larger gap compared to the case of 4 T, while for 6 and 6.5 T the gap decreases. At the same time, we find tens of energy bands in the energy window of $\varepsilon \lesssim 2$ K, while its number seems to decrease with increasing the field. This will influence the number of magnon carriers thermally excited, and explain the continuous decrease of κ_{xx} in the experiment toward 8 T.

For κ_{xy}/T , not only the number of low energy bands but the sign of Ω_{xy}^n matters, which cannot be visibly understood solely by the present plot, and will be examined in the next subsection.

3. Degree of contributions from magnon bands to κ_{xy}

We now examine how the variation of energy bands influences κ_{xy} by examining their contribution in detail. The

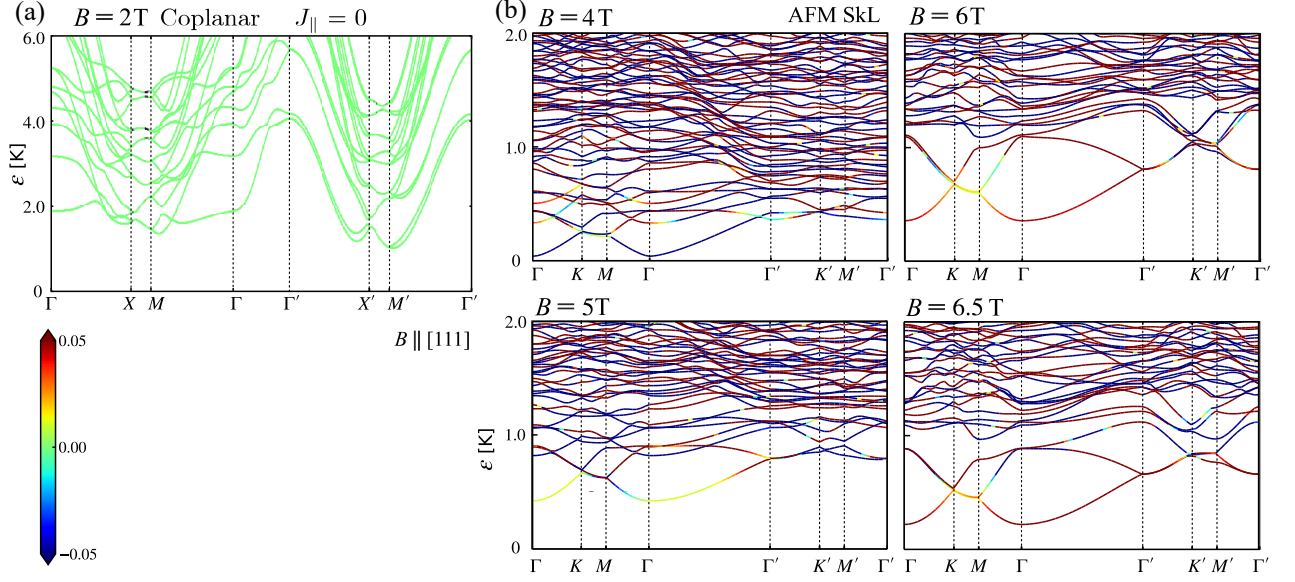


FIG. 10. Magnon bands obtained by the spin-wave theory in a field $\mathbf{B} \parallel [111]$. (a) Coplanar state at $B = 2\text{ T}$ and $J_{\parallel} = 0$ to be compared with the helical state in Fig. 3(a), both with $N_c = 16$. (b-d) AFM-SkL state with $N_c = 384$ at $B = 4, 5, 6, 6.5\text{ T}$. Energy bands are shown in the color density plot of the Berry curvature $\Omega_{xy}^{(n)}$. The case of $\Omega_{xy}^{(n)} > 0.05$ and < -0.05 are all plotted in red and blue, respectively.

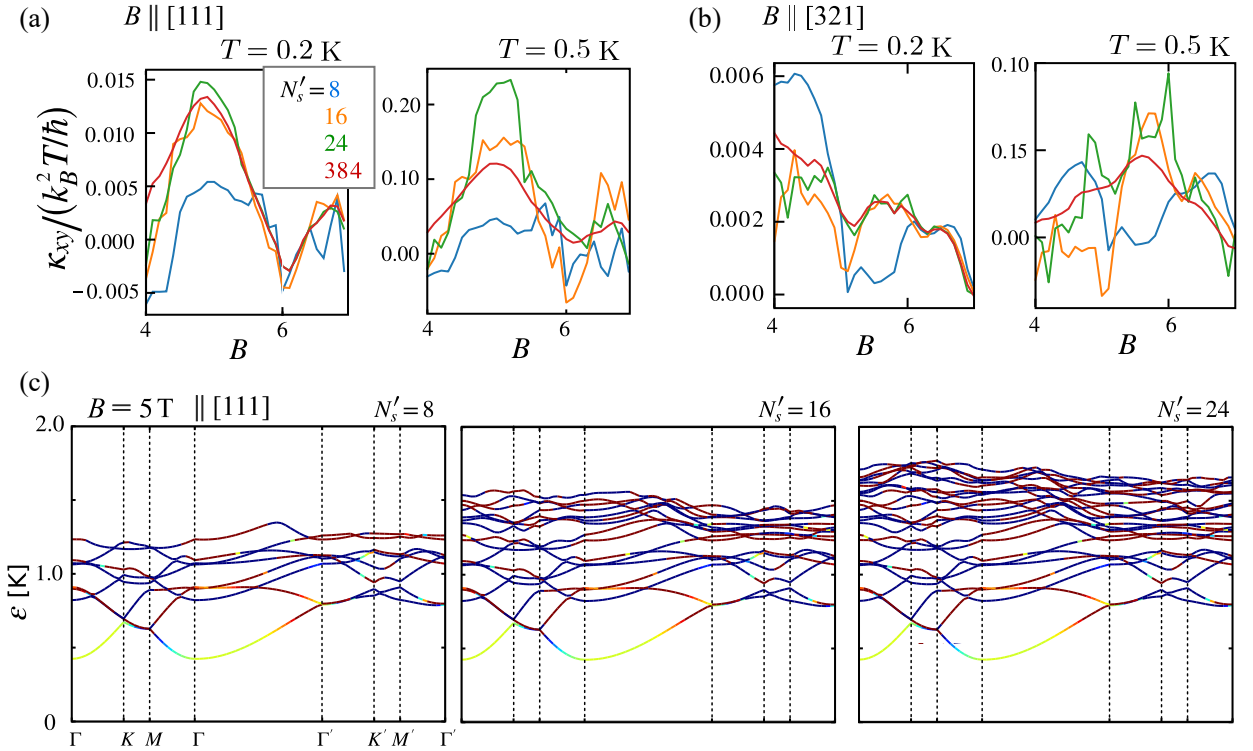


FIG. 11. (a,b) $\kappa_{xy} / (k_B^2 T / \hbar)$ of the AFM-SkL phase obtained using the lowest N'_s -bands ($N'_s = 8, 16, 24, 384$) in taking the integral in for the field directions $\mathbf{B} \parallel [111]$ and $[321]$. (c) The description of lowest N'_s bands ($N'_s = 8, 16, 24$) at $B = 5\text{ T}$ and $\mathbf{B} \parallel [111]$.

Berry curvature $\Omega_{\mu\nu}^{(n)}(\mathbf{k})$ ($n = 1, 2, \dots, N_s$) is described as

$$\begin{aligned}\Omega_{\mu\nu}^{(n)}(\mathbf{k}) &= -2\text{Im} \left[\frac{\partial t_n^\dagger(\mathbf{k})}{\partial k_\mu} \Sigma^z \frac{\partial t_n(\mathbf{k})}{\partial k_\nu} \right] \\ &= -2 \sum_{m=1}^{2N_s} (1 - \delta_{m,n}) (\Sigma^z)_{m,m} \\ &\frac{\text{Im} \left[t_n^\dagger(\mathbf{k}) \frac{\partial H_{\text{BdG}}(\mathbf{k})}{\partial k_\mu} t_m(\mathbf{k}) t_m^\dagger(\mathbf{k}) \frac{\partial H_{\text{BdG}}(\mathbf{k})}{\partial k_\nu} t_n(\mathbf{k}) \right]}{(\varepsilon_n(\mathbf{k}) - \varepsilon_m(\mathbf{k}))^2 + \delta},\end{aligned}\quad (\text{B11})$$

where $m = N_s + 1, \dots, 2N_s$ denotes the particle-hole pairs. The first line in Eq.(B11) gives the expressions using only the information about the n -th band, while the second expression includes the inter-band matrix elements over the whole bands, making use of the completeness of the basis. We use the latter for numerical evaluation, where we introduce an infinitesimal positive number δ to reduce the numerical error due to divergence and take $\delta \rightarrow 0$.

We now test how the number of bands included in the calculation of κ_{xy} , denoted as N'_s would influence the results. After obtaining the distribution of $\Omega_{xy}^{(n)}(\mathbf{k})$ over all the magnon bands, we confine the summation to the lowest N'_s -bands in the following formula,

$$\kappa_{xy} = -\frac{k_B^2 T}{\hbar} \int_{\text{BZ}} \frac{d^3 \mathbf{k}}{(2\pi)^3} \sum_{n=1}^{N'_s} c_2 [f(\varepsilon_n(\mathbf{k}))] \Omega_{xy}^{(n)}(\mathbf{k}). \quad (\text{B12})$$

Figure 11(a) shows κ_{xy} as function of $\mathbf{B} \parallel [111]$ for different choices of $N'_s = 8, 16, 24$ and 384(full) at $T = 0.2$ and 0.5 K. At $T = 0.2$ K, the results converge already at $N'_s = 16$, showing that only 10 bands or so contribute to κ_{xy} . However, at $T = 0.5$ K, the results differ much even when we increase as large as $N'_s = 24$. The same tendency holds for $\mathbf{B} \parallel [321]$ shown in Fig. 11(b). For clarification, we plot in Fig. 11(c) the lowest N'_s -bands with $N'_s = 8, 16, 24$. One finds that already at $T = 0.5$ K, the magnon excitation following Bose statistics easily exceeds the energy window ~ 2 K that accomodates $N'_s = 24$. We thus clarify that in the AFM-SkL phase, the characteristic dense magnon energy bands contribute up to high energies in the thermal Hall effect.

4. Real-space spin texture and U(1) gauge fields in AFM-SkX on the triangular lattice

Here, we give the details of the calculations performed to obtain Fig. 4 in the main text. We consider the two-dimensional xy -plane that describes a single [111]-layer of MnSc_2S_4 that form the triangular lattice by taking [111] as z -axis. The orientations of the ordered magnetic moments of the AFM-SkL (see Fig. 1 and Fig. 4(e) in the main text) is given by the unit vector $\mathbf{m}(\mathbf{r})$ whose

elements are given in the Cartesian coordinate as

$$\begin{aligned}\mathbf{m}(\mathbf{r}) &= A^{-1} \left(\sum_{m=1}^3 \left(-\sin(\mathbf{q}_m \cdot \mathbf{r}) \mathbf{e}^m + \cos \left(\mathbf{q}_m \cdot \mathbf{r} - \frac{9\pi}{8} \right) \mathbf{e}^z \right) \right. \\ &\quad \left. + M \mathbf{e}^z \right)\end{aligned}\quad (\text{B13})$$

where A is a normalization factor to keep $|\mathbf{m}(\mathbf{r})| = 1$, M is the spatially uniform magnetization due to a finite magnetic field, and \mathbf{e}_m ($m = 1, 2, 3$) are the unit vectors on the three-dimensional plane pointing in the direction perpendicular to \mathbf{q}_m as

$$\begin{aligned}\mathbf{e}^1 &= -\frac{\sqrt{3}}{2} \mathbf{e}^x - \frac{1}{2} \mathbf{e}^y, \quad \mathbf{e}^2 = -\mathbf{e}^y, \quad \mathbf{e}^3 = \frac{\sqrt{3}}{2} \mathbf{e}^x - \frac{1}{2} \mathbf{e}^y \\ \mathbf{q}_1 &= \frac{3\pi}{2} \left(\frac{1}{2} \mathbf{e}_x - \frac{\sqrt{3}}{2} \mathbf{e}_y \right), \quad \mathbf{q}_2 = \frac{3\pi}{2} \mathbf{e}_x, \quad \mathbf{q}_3 = \frac{3\pi}{2} \left(\frac{1}{2} \mathbf{e}_x + \frac{\sqrt{3}}{2} \mathbf{e}_y \right)\end{aligned}\quad (\text{B14})$$

where we regard \mathbf{e}^μ and \mathbf{e}_μ as those defined in the spin space and in real space, respectively (see Fig. 12(a)).

Let us consider the spatial variation of magnetic moments separately for the three sublattices $\ell = A, B, C$ to construct the U(1) gauge fields. This can be done by using the same \mathbf{e}_m ($m = 1, 2, 3$) as those given in Eq.(B14) but by taking different periods of propagation vectors

$$\mathbf{Q}_1 = \frac{\pi}{6} \left(\frac{1}{2} \mathbf{e}_x - \frac{\sqrt{3}}{2} \mathbf{e}_y \right), \quad \mathbf{Q}_2 = \frac{\pi}{6} \mathbf{e}_x, \quad \mathbf{Q}_3 = \frac{\pi}{6} \left(\frac{1}{2} \mathbf{e}_x + \frac{\sqrt{3}}{2} \mathbf{e}_y \right)\quad (\text{B16})$$

and by shifting the origin depending on the sublattices to $\tilde{\mathbf{r}}_\ell = \mathbf{r} - \mathbf{r}_0^\ell$ with $\mathbf{r}_0^A = 0$, $\mathbf{r}_0^B = (16, 0)$, $\mathbf{r}_0^C = (8, 0)$, we find

$$\begin{aligned}\mathbf{m}_\ell(\mathbf{r}) &= A^{-1} \left(\sum_{m=1}^3 \left(-\sin(\mathbf{Q}_m \cdot \tilde{\mathbf{r}}_\ell) \mathbf{e}^m + \cos \left(\mathbf{Q}_m \cdot \tilde{\mathbf{r}}_\ell - \frac{9\pi}{8} \right) \mathbf{e}^z \right) \right. \\ &\quad \left. + M \mathbf{e}^z \right)\end{aligned}\quad (\text{B17})$$

Since $\mathbf{m}_\ell(\mathbf{r})$ is described using $(\theta_\ell(\mathbf{r}), \phi_\ell(\mathbf{r}))$, we can rewrite these elements as

$$\begin{aligned}\sin \theta_\ell(\mathbf{r}) \cos \phi_\ell(\mathbf{r}) &= \frac{\sqrt{3}}{2A} \left(\sin(\mathbf{Q}_1 \cdot \tilde{\mathbf{r}}_\ell) - \sin(\mathbf{Q}_3 \cdot \tilde{\mathbf{r}}_\ell) \right) \\ \sin \theta_\ell(\mathbf{r}) \sin \phi_\ell(\mathbf{r}) &= \frac{-1}{2A} \left(\sin(\mathbf{Q}_1 \cdot \tilde{\mathbf{r}}_\ell) + 2 \sin(\mathbf{Q}_2 \cdot \tilde{\mathbf{r}}_\ell) + \sin(\mathbf{Q}_3 \cdot \tilde{\mathbf{r}}_\ell) \right) \\ \cos \theta_\ell(\mathbf{r}) &= \frac{1}{A} \left(\sum_m \cos \left(\mathbf{Q}_m \cdot \tilde{\mathbf{r}}_\ell - \frac{9\pi}{8} \right) + M \right),\end{aligned}\quad (\text{B18})$$

which gives the description of magnetic moments in the continuous space \mathbf{r} in the xy plane. Figure 12(b) shows the comparison of $\mathbf{m}(\mathbf{r})$ in Eq.(B13) and $\mathbf{m}_\ell(\mathbf{r})$ in Eq.(B17) along the $\mathbf{r}_j = (x_j, 0)$ line calculated for discrete lattice points where we set $M = 0$. At each lattice point, they cross while the spatial periods for the continuous \mathbf{r} differ. This shows that the two equations are consistent with each other.

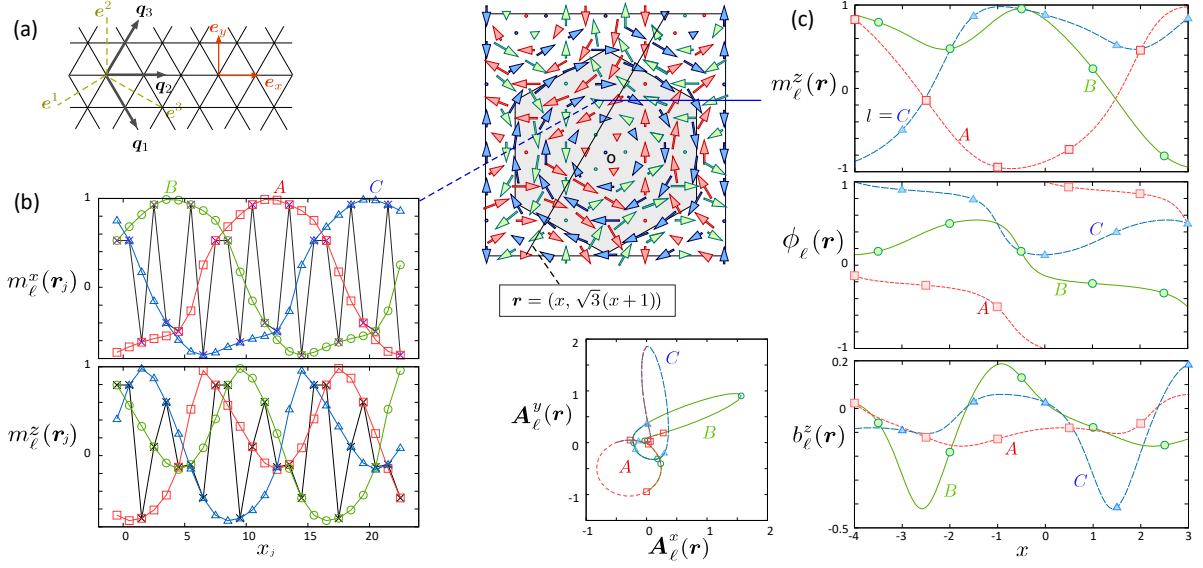


FIG. 12. (a) Vectors defined in the two-dimensional xy -plane used in the formulation. (b) Magnetic structures $m_\ell^x(\mathbf{r}_j)$ and $m_\ell^z(\mathbf{r}_j)$ obtained for discrete lattice sites $\mathbf{r}_j = (x_j, 3\sqrt{3}/2)$. The one using Eq.(B13) give the magnetization for all three sublattices, whereas those in Eq.(B17) give \mathbf{m}_ℓ of $\ell = A, B$, and C sublattices separately, showing that the two equations are consistent. (c) The magnetization $m_\ell^z(\mathbf{r})$, $\phi_\ell(\mathbf{r})$, and $b_\ell^z(\mathbf{r})$ along the $\mathbf{r} = (x, \sqrt{3}(x+1))$ line. The data points are the values for the discrete lattice points, and the lines are the obtained as continuous functions of \mathbf{r} . The corresponding $\theta_\ell(\mathbf{r})$ and $m_\ell^x(\mathbf{r}), m_\ell^y(\mathbf{r})$ are given in Fig. 4 in the main text. The variation of vector potential is given on the plane of $A_\ell^x(\mathbf{r})$ and $A_\ell^y(\mathbf{r})$.

The U(1) gauge field is constructed using slowly varying sets of $\mathbf{m}_\ell(\mathbf{r})$. The vector potential for the three sublattices is given as

$$\mathbf{A}_\ell(\mathbf{r}) = -\frac{\cos \phi_\ell(\mathbf{r})}{\tan \theta_\ell(\mathbf{r})} \nabla \mathbf{m}_\ell^y(\mathbf{r}) + \frac{\sin \phi_\ell(\mathbf{r})}{\tan \theta_\ell(\mathbf{r})} \nabla \mathbf{m}_\ell^x(\mathbf{r}), \quad (\text{B19})$$

and the fictitious magnetic field generated as a rotation of the vector field $\mathbf{A}_\ell(\mathbf{r})$ is given as

$$b_\ell^z(\mathbf{r}) = \partial_x A_\ell^y(\mathbf{r}) - \partial_y A_\ell^x(\mathbf{r}) = \mathbf{m}_\ell(\mathbf{r}) \cdot (\partial_x \mathbf{m}_\ell(\mathbf{r}) \times \partial_y \mathbf{m}_\ell(\mathbf{r})), \quad (\text{B20})$$

where

$$\begin{aligned} \partial_\mu \mathbf{m}_\ell^x(\mathbf{r}) &= \frac{\sqrt{3}}{2A} \left((\mathbf{Q}_1)_\mu \cos(\mathbf{Q}_1 \cdot \tilde{\mathbf{r}}_\ell) - (\mathbf{Q}_3)_\mu \cos(\mathbf{Q}_3 \cdot \tilde{\mathbf{r}}_\ell) \right), \\ \partial_\mu \mathbf{m}_\ell^y(\mathbf{r}) &= \frac{1}{2A} \left((\mathbf{Q}_1)_\mu \cos(\mathbf{Q}_1 \cdot \tilde{\mathbf{r}}_\ell) + 2(\mathbf{Q}_2)_\mu \cos(\mathbf{Q}_2 \cdot \tilde{\mathbf{r}}_\ell) \right. \\ &\quad \left. + (\mathbf{Q}_3)_\mu \cos(\mathbf{Q}_3 \cdot \tilde{\mathbf{r}}_\ell) \right), \\ \partial_\mu m_\ell^z(\mathbf{r}) &= -\frac{1}{A} \left[\sum_m (\mathbf{Q}_m)_\mu \sin(\mathbf{Q}_m \cdot \tilde{\mathbf{r}}_\ell - \frac{9\pi}{8}) \right]. \end{aligned} \quad (\text{B21})$$

Figure 12 (c) shows $m_\ell^z(\mathbf{r})$, $\phi_\ell(\mathbf{r})$ and $b_\ell^z(\mathbf{r})$ separately for the three sublattices. They are the continuous functions of \mathbf{r} where we put the symbols at the discrete lattice points. The corresponding data of $\theta_\ell(\mathbf{r})$ and $m_\ell^x(\mathbf{r}), m_\ell^y(\mathbf{r})$ profile are shown in Fig. 4 in the main text.

* takeda.hikaru@issp.u-tokyo.ac.jp

† masataka.kawano@tum.de

¹ Coldea, R. *et al.* Quantum criticality in an ising chain: Experimental evidence for emergent E_8 symmetry. *Science*

327, 177 (2010).

² Zamolodchikov, A. Integrals of motion and s-matrix of the (scaled) $T = T_c$ ising model with magnetic field. *International Journal of Modern Physics A* **4**, 4235 (1989).

- ³ Kitaev, A. Anyons in an exactly solved model and beyond. *Ann. Phys.* **321**, 2 (2006).
- ⁴ Kasahara, Y. *et al.* Majorana quantization and half-integer thermal quantum Hall effect in a Kitaev spin liquid. *Nature* **559**, 227–231 (2018).
- ⁵ Yamashita, M., Gouchi, J., Uwatoko, Y., Kurita, N. & Tanaka, H. Sample dependence of half-integer quantized thermal Hall effect in the Kitaev spin-liquid candidate α -RuCl₃. *Physical Review B* **102**, 220404 (2020).
- ⁶ Yokoi, T. *et al.* Half-integer quantized anomalous thermal Hall effect in the Kitaev material candidate α -RuCl₃. *Science* **373**, 568–572 (2021).
- ⁷ Bruin, J. a. N. *et al.* Robustness of the thermal Hall effect close to half-quantization in α -RuCl₃. *Nature Physics* **18**, 401–405 (2022).
- ⁸ Kimura, K. *et al.* Quantum fluctuations in spin-ice-like Pr₂Zr₂O₇. *Nature Comm.* **4**, 1934 (2013).
- ⁹ Neubauer, A. *et al.* Topological Hall Effect in the A Phase of MnSi. *Phys. Rev. Lett.* **102**, 186602 (2009).
- ¹⁰ Lee, M., Kang, W., Onose, Y., Tokura, Y. & Ong, N. P. Unusual Hall Effect Anomaly in MnSi under Pressure. *Phys. Rev. Lett.* **102**, 186601 (2009).
- ¹¹ Kanazawa, N. *et al.* Large Topological Hall Effect in a Short-Period Helimagnet MnGe. *Phys. Rev. Lett.* **106**, 156603 (2011).
- ¹² Li, Y. *et al.* Robust Formation of Skyrmions and Topological Hall Effect Anomaly in Epitaxial Thin Films of MnSi. *Phys. Rev. Lett.* **110**, 117202 (2013).
- ¹³ Mühlbauer, S. *et al.* Skyrmion lattice in a chiral magnet. *Science* **323**, 915–919 (2009).
- ¹⁴ Yu, X. Z. *et al.* Real-space observation of a two-dimensional skyrmion crystal. *Nature* **465**, 901–904 (2010).
- ¹⁵ Tokura, Y. & Kanazawa, N. Magnetic skyrmion materials. *Chem. Rev.* **121**, 2857 (2007).
- ¹⁶ Nagaosa, N. & Tokura, Y. Topological properties and dynamics of magnetic skyrmions. *Nature Nanotechnology* **8**, 899 (2013).
- ¹⁷ Onose, Y. *et al.* Observation of the magnon Hall effect. *Science* **329**, 297–299 (2010).
- ¹⁸ Fujimoto, S. Hall effect of spin waves in frustrated magnets. *Phys. Rev. Lett.* **103**, 047203 (2009).
- ¹⁹ Katsura, H., Nagaosa, N. & Lee, P. A. Theory of the thermal Hall effect in quantum magnets. *Phys. Rev. Lett.* **104**, 066403 (2010).
- ²⁰ Matsumoto, R. & Murakami, S. Rotational motion of magnons and the thermal Hall effect. *Phys. Rev. B* **84**, 184406 (2011).
- ²¹ Matsumoto, R. & Murakami, S. Theoretical Prediction of a Rotating Magnon Wave Packet in Ferromagnets. *Phys. Rev. Lett.* **106**, 197202 (2011).
- ²² Akazawa, M. *et al.* Topological thermal Hall effect of magnons in magnetic skyrmion lattice. *Phys. Rev. Res.* **4**, 043085 (2022).
- ²³ van Hoogdalem, K. A., Tserkovnyak, Y. & Loss, D. Magnetic texture-induced thermal Hall effects. *Phys. Rev. B* **87**, 024402 (2013).
- ²⁴ Gao, S. *et al.* Fractional antiferromagnetic skyrmion lattice induced by anisotropic couplings. *Nature* **586**, 37 (2020).
- ²⁵ Gao, S. *et al.* Spiral spin-liquid and the emergence of a vortex-like state in MnSc₂S₄. *Nature Phys.* **13**, 157 (2017).
- ²⁶ Kawano, M., Onose, Y. & Hotta, C. Designing Rashba-Dresselhaus effect in magnetic insulators. *Commun. Phys.* **2**, 27 (2019).
- ²⁷ Kawano, M. & Hotta, C. Thermal Hall effect and topological edge states in a square-lattice antiferromagnet. *Phys. Rev. B* **99**, 054422 (2019).
- ²⁸ Kawano, M. & Hotta, C. Discovering momentum-dependent magnon spin texture in insulating antiferromagnets: Role of the Kitaev interaction. *Phys. Rev. B* **100**, 174402 (2019).
- ²⁹ Fritsch, V. *et al.* Spin and orbital frustration in MnSc₂S₄ and FeSc₂S₄. *Phys. Rev. Lett.* **92**, 116401 (2004).
- ³⁰ Reil, S., Stork, H.-J. & Haeuselner, H. Structural investigations of the compounds ASc₂S₄ (A = Mn, Fe, Cd). *Journal of Alloys and Compounds* **334**, 92 (2002).
- ³¹ Bergman, D., Alicia, J., Gull, E., Trebst, S. & Balents, L. Order-by-disorder and spiral spin-liquid in frustrated diamond-lattice antiferromagnets. *Nature Phys.* **3**, 487 (2007).
- ³² Rosales, H. D., Cabra, D. C. & Pujol, P. Three-sublattice skyrmion crystal in the antiferromagnetic triangular lattice. *Phys. Rev. B* **92**, 214439 (2015).
- ³³ Rosales, H. D. *et al.* Anisotropy-driven response of the fractional antiferromagnetic skyrmion lattice in MnSc₂S₄ to applied magnetic fields. *Phys. Rev. B* **105**, 224402 (2022).
- ³⁴ Göbel, B., Mook, A., Henk, J. & Mertig, I. Antiferromagnetic skyrmion crystals: Generation, topological Hall, and topological spin Hall effect. *Phys. Rev. B* **96**, 060406 (2017).
- ³⁵ Berman, R. *Thermal Conduction in Solids* (Clarendon, Oxford, 1976).
- ³⁶ Streib, S., Vidal-Silva, N., Shen, K. & Bauer, G. E. W. Magnon-phonon interactions in magnetic insulators. *Phys. Rev. B* **99**, 184442 (2019).
- ³⁷ Zhitomirsky, M. E. & Chernyshev, A. L. Colloquium: spontaneous magnon decays. *Rev. Mod. Phys.* **85**, 219–242 (2013).
- ³⁸ Chernyshev, A. L. & Maksimov, P. A. Damped topological magnons in the kagome-lattice ferromagnets. *Phys. Rev. Lett.* **117**, 187203 (2016).
- ³⁹ Li, X., Fauqué, B., Zhu, Z. & Behnia, K. Phonon thermal Hall effect in strontium titanate. *Physical Review Letters* **124**, 105901 (2020).
- ⁴⁰ Grissonnanche, G. *et al.* Chiral phonons in the pseudogap phase of cuprates. *Nature Physics* **16**, 1108–1111 (2020).
- ⁴¹ Akazawa, M. *et al.* Thermal Hall effects of spins and phonons in kagome antiferromagnet Cd-Kapellasite. *Physical Review X* **10**, 041059 (2020).
- ⁴² Roldán-Molina, A., Nunez, A. S. & Fernández-Rossier, J. Topological spin waves in the atomic-scale magnetic skyrmion crystal. *New Journal of Physics* **18**, 045015 (2016).
- ⁴³ Díaz, S. A., Hirose, T., Klinovaja, J. & Loss, D. Chiral magnonic edge states in ferromagnetic skyrmion crystals controlled by magnetic fields. *Phys. Rev. Res.* **2**, 013231 (2020).
- ⁴⁴ Garst, M., Waizner, J. & Grundler, D. Collective spin excitations of helices and magnetic skyrmions: review and perspectives of magnonics in non-centrosymmetric magnets. *Journal of Physics D: Applied Physics* **50**, 293002 (2017).
- ⁴⁵ Holstein, T. & Primakoff, H. Field dependence of the intrinsic domain magnetization of a ferromagnet. *Phys. Rev.* **58**, 1098–1113 (1940).
- ⁴⁶ Colpa, J. H. P. Diagonalization of the quadratic boson hamiltonian. *Physica A* **93**, 327–353 (1978).
- ⁴⁷ Matsumoto, R., Shindou, R. & Murakami, S. Thermal

- Hall effect of magnons in magnets with dipolar interaction. *Phys. Rev. B* **89**, 054420 (2014).
- ⁴⁸ McClarty, P. A. *et al.* Topological magnons in Kitaev magnets at high fields. *Phys. Rev. B* **98**, 060404(R) (2018).
- ⁴⁹ Kim, S. K., Nakata, K., Loss, D. & Tserkovnyak, Y. Tunable magnonic thermal Hall effect in skyrmion crystal phases of ferrimagnets. *Phys. Rev. Lett.* **122**, 057204 (2019).
- ⁵⁰ Roldan-Molina, A., Nunez, A. S. & Fernandez-Rossier, J. Topological spin waves in the atomic-scale magnetic skyrmion crystal. *New Journal of Physics* **18**, 045015 (2016).
- ⁵¹ Rashba, E. I. Properties of semiconductors with an extremum loop. 1. Cyclotron and combinational resonance in a magnetic field perpendicular to the plane of the loop. *Sov. Phys. Solid State* **2**, 1224–1238 (1960).
- ⁵² Molina, R. A., Dukelsky, J. & Schmitteckert, P. Crystallization of trions in SU(3) cold-atom gases trapped in optical lattices. *Phys. Rev. A* **80**, 013616 (2009).
- ⁵³ Yamamoto, D., Suzuki, C., Marmorini, G., Okazaki, S. & Furukawa, N. Quantum and thermal phase transitions of the triangular SU(3) heisenberg model under magnetic fields. *Phys. Rev. Lett.* **125**, 057204 (2020).
- ⁵⁴ Münzer, W. *et al.* Skyrmion lattice in the doped semiconductor $fe_{1-x}Co_xSi$. *Phys. Rev. B* **81**, 041203 (2010).
- ⁵⁵ Oike, H. *et al.* Interplay between topological and thermodynamic stability in a metastable magnetic skyrmion lattice. *Nature Physics* **12**, 62–66 (2016).
- ⁵⁶ Okamura, Y., Kagawa, F., Seki, S. & Tokura, Y. Transition to and from the skyrmion lattice phase by electric fields in a magnetoelectric compound. *Nature Communications* **7**, 12669 (2016).
- ⁵⁷ Bauer, A., Garst, M. & Pfleiderer, C. History dependence of the magnetic properties of single-crystal $Fe_{1-x}Co_xSi$. *Phys. Rev. B* **93**, 235144 (2016).
- ⁵⁸ Chauhan, H. C., Kumar, B. & Ghosh, S. Origin of metamagnetism in skyrmion host Cu_2OSeO_3 . *Scientific Reports* **12**, 15971 (2022).